Pamukkale Üniversitesi Mühendislik Bilimleri Dergisi
Pamukkale University Journal of Engineering Sciences

Experimental verification of performance of single phase induction motor for different rotor slot shapes

Farklı rotor oluk şekilleri için bir fazlı asenkron motor performansının deneysel doğrulanması

Merve ŞEN KURT[1], Ahmet FENERCİOĞLU[2]*

[1]Department of Electrical and Electronics Engineering, Amasya University, Amasya, Türkiye.
merve.sen@amasya.edu.tr
[2]Department of Mechatronics Engineering, Bursa Technical University, Bursa, Türkiye.
ahmet.fenercioglu@btu.edu.tr

Received/Geliş Tarihi: 20.06.2022 Revision/Düzeltme Tarihi: 13.08.2024 doi: 10.5505/pajes.2024.95769
Accepted/Kabul Tarihi: 03.12.2024 Research Article/Araştırma Makalesi

Abstract

This study investigates the effect of rotor slot design and the improvement to performance and efficiency in the run capacitor single phase induction motor used in refrigerator compressor. The study considers the effect of deep and double cage rotor slot design on performance and compares this with the original motor design using finite element analysis. Rotors with deep and double cage slot structure were manufactured as prototypes and tested in the same stator. The reliability of the model was confirmed by the experimental measurements and finite element analysis solutions. The efficiency of the motor was increased by 4.1% with the double cage rotor and 1.95% with the deep slot structure with improvements in rotor slot geometry. The best performance from the double cage rotor induction motors was output power 125 W, torque 0.42 Nm, speed 2932 rpm, power factor 0.94, and 77% efficiency.

Keywords: FEA, Rotor geometry, Induction motor

Öz

Bu çalışmada; buzdolabı kompresöründe kullanılan daimi kapasitörlü bir fazlı asenkron motorun rotor oluk tasarımında yapılacak iyileştirmeler ile elektriksel ve mekaniksel performansının ve veriminin arttırılması amaçlanmıştır. Çalışma, derin ve çift kafesli rotor yuvası tasarımının performans üzerindeki etkisini dikkate almakta ve bunu sonlu elemanlar analizi kullanılarak orijinal motor tasarımıyla karşılaştırmaktadır. Derin oluk ve çift kafesli oluk yapısına sahip rotorların prototip olarak imal edilerek aynı stator içerisinde test edilmiştir. Test sonuçları ve sonlu elemanlar analiz sonuçları karşılaştırılarak modelin güvenilirliği teyit edilmiştir. Rotor oluk geometrisinde yapılan iyileştirmeler sonucunda orijinal rotora göre çift kafesli rotor ile motorun verimi %4.1, derin oluk yapısı ile verim %1.95 artırılmıştır. Bir fazlı asenkron motorun manyetik akı, akım yoğunlukları ve sargı sıcaklıkları dikkate alınarak etiket değerleri yeniden belirlenmiştir. Buna göre çift kafes yapılı rotora sahip motorun çıkış gücü 125 W, anma torku 0.42 Nm, anma hızı 2932 d/d, güç faktörü 0.94 ve verim %77 olarak belirlenmiştir.

Anahtar kelimeler: SEY, Rotor geometrisi, İndüksiyon motor

1 Introduction

Single phase induction motors (SPIMs) are cheap in cost, simple and robust in construction, reliable and easy to repair. Due to all these advantages, they nowadays are widely used in domestic and commercial areas [1]-[3].

In induction motors, high starting torque (high rotor resistance) and low current (high rotor reactance) are required when the motor starts. In steady-state operation, low rated slip and high efficiency (low rotor resistance and reactance) are required. The most essential way to achieve this is to create 2 parallel paths in the design through which rotor current can flow [4]. One of the parallel paths has high rotor resistance and reactance, whereas the second parallel path has low rotor resistance and reactance. When the motor starts, the rotor frequency is high and the rotor impedance is frequency dependent and it increases during start-up due to skin effect at high frequency. In steady-state operation, since rotor frequency is low, impedance is also low. In this way, the inrush current is dragged down whereas in steady-state operation, the decrease of motor efficiency is avoided. Variable rotor resistance can be achieved by

designing the deep or double cage rotor slot structure in SPIM. Figure 1 shows the deep slot and double cage rotor slot structure, respectively.

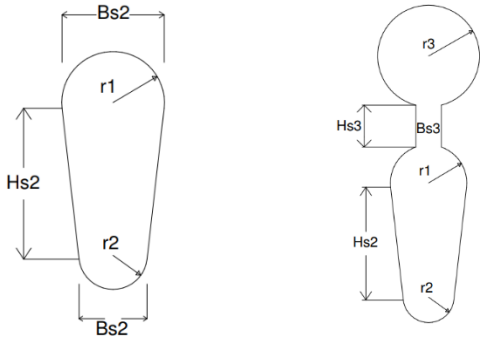

(a) (b)

Figure 1. The rotor slot structure of SPIM (a) deep slot and (b) double cage

*Corresponding author/Yazışılan Yazar

The original motor of this study is used in refrigerator compressor and has the characteristics; 96 W output power, 0.31 Nm nominal torque, 2950 rpm speed and 72% efficiency. 2D model of the original motor model designed in the Ansys / Maxwell software (Figure 2).

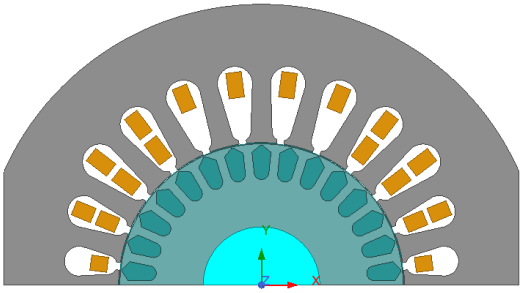

Figure 2. Cross section of original motor

Previous studies have shown that use of the deep slot and double cage rotor slot structure to improve motor performance affects each of the motor performance variables differently. National Electrical Manufacturers Association (NEMA) design examples show that different torque-speed characteristics can be achieved with changes in the design of the rotor slot [4]. Some of the studies in the literature on this subject are given below.

One study [5] reviews studies that have investigated the effect of rotor slot geometry on the performance of a single-phase induction motor (SPIM) and concludes that the dimension and shape of the rotor slot, number of slots, core material, rotor windings, and slot opening have significant effect on the performance (efficiency, torque, power, etc.) of the asynchronous motor.

Another study [6] shows an increase in slot depth, without change in rotor slot area, increases the starting torque, but leads to a reduction in maximum torque and starting/operating current. In addition, due to the reduction in the locked rotor torque arising from the increase in the rotor slot depth [7].

One study concluded that increasing the cross-section of the rotor slot increases the maximum torque while decreasing the operating torque for two motor types, 400 W and 250 W. This situation caused an increase in the starting current of the motor. The best results were achieved when the slot width was reduced and the height increased on both motors. This study differs from other studies by discussing the effect of rotor slot geometry on magnetic field density. In both motors with optimal rotor slot geometry, the magnetic fields were observed to be formed as circular due to the improvement of motor performance [8].

Another study concluded that when the depth of the rotor slot is increased, the starting torque increases and the starting current decreases, and optimal rotor slot depth was achieved in the 3 models of motor studied [9].

This study investigates modifications to the design of the rotor slot in a SPIM with conical shape rotor using the Ansys / Maxwell environment for simulation. In recent papers in the literature, some papers compare the original rotor with a deep slot rotor, while others compare it with a double cage rotor. In this study, unlike previous publications, we first compared the original rotor slot with the optimal deep slot structure, then the original rotor slot with the double cage deep slot structure, and finally, the optimal deep slot with the double cage design. This study was a unique study in that it handled both deep slot and double cage rotor slot geometry design studies together.

Three designs based on previous studies [10]-[12] were modelled; original motor (Model A), optimal deep slot (Model B), and optimal double cage rotor slot (Model C). For all models, all aspects of the rotor core, stator core and windings were kept the same, and the cross-sectional area of the rotor bars was maintained as constant as possible. For this purpose, in models with different rotor slot geometries, the total rotor slot area (A_r) was constant without affecting the parallelism of the rotor slot teeth. Each of the models was analyzed using the finite element method. Prototype rotors were made and installed in the motor and tests performed.

2 Material and method

For the two parallel paths created in the variable resistance rotor slot design the majority of the current at the initial time, when the rotor frequency is comparatively high, will prefer the high resistance path due to skin effect, and in steady-state operation it will pass through the low resistance section. Focusing on design of the variable resistance rotor bar, in order to take advantage of the skin effect, the minimum value that is computed by using Equation (1). In this equation δ, ρ_{br}, f and μ_0 refer to the least skin effect depth, specific resistance (Ω.m), frequency (Hz), and magnetic permeability of the airgap (H/m), respectively [13].

$$\delta = \sqrt{\frac{\rho_{br}}{\mu_0 \pi f}} \qquad (1)$$

2.1 Deep slot rotor geometry

The deep slot rotor geometry (Figure 1(a)) provides the condition that the rotor resistance varies with frequency; the effective value of the rotor resistance during high frequency starting is several times the rotor resistance during steady-state operation. This leads to initially high rotor resistance which diminishes as speed increases, thereby facilitating high torque at startup without compromising motor efficiency during steady-state operation. The deep slot rotor structure and equivalent circuit are presented in Figure 3(a) and Figure 3(b), respectively. In the equivalent circuit, R_r indicates the rotor bar resistance, whereas X_r indicates the rotor bar reactance and X_m is the mutual inductance between the lower and upper bar.

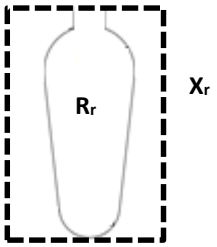

(a)

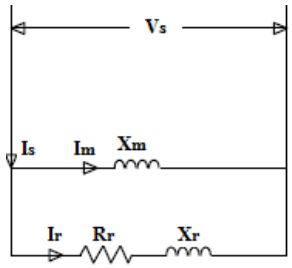

(b)

Figure 3. (a) Deep slot rotor and (b) Rotor equivalent circuit

Rotor bar resistance and inductance are playing an important role in the performance of SPIMs. Rotor bar inductance (L_b) in a motor with deep slot rotor structure is expressed by Equation (2). In this equation μ_0, l_{br}, N_r and λ_b refer respectively to the magnetic permeability of the airgap, rotor bar length, the number of rotor slots and the rotor bar coefficient [13].

$$L_b = \mu_0 . l_{br} . N_r^2 . \lambda_b \quad (2)$$

The rotor bar coefficient of permeability (λ_b) is a variable that depends on the slot depth or height (H_{s2}) in Equation (3). k_2 in Equation (3) is a constant for the deep slot ($0.645 < k_2 < 0.785$) and k_1 ($k_1 < 1$) refers to the inductance attenuation factor. In Equation (3), B_{s1}, h_{or} and B_{s0} define the lower width of the rotor slot, rotor slot mouth height, and the rotor slot opening, respectively. A smaller rotor bar coefficient of permeability will result in a lower value of rotor bar inductance, as seen in Equation (2).

$$\lambda_b = \frac{H_{s2}}{3B_{s1}} k_1 + k_2 - \frac{h_{or}}{2B_{s1}} + \frac{h_{or}}{B_{so}} \quad (3)$$

The rotor bar inductance from Equation (2) may be used to calculate rotor bar reactance, as X_r in Equation (4).

$$X_r = 2\pi f L_b \quad (4)$$

Rotor bar impedance (Z_r) is calculated using Equation (5), where s indicates the slip parameter.

$$Z_r = \frac{R_r}{s} + jX_r \quad (5)$$

The total impedance of the rotor circuit (Z_t) is calculated using Equation (6), where R_{sm} and X_{sm} are the stator main winding resistance and leakage reactance, respectively.

$$Z_t = \frac{Z_r . X_m}{Z_r + X_m} + R_{sm} + jX_{sm} \quad (6)$$

The input current (I_s) is calculated using the total impedance (Z_t) of the rotor circuit and the phase voltage (V_s), as in Equation (7).

$$I_s = \frac{V_s}{Z_t} \quad (7)$$

2.2 Double cage rotor geometry

A second approach to make rotor bar resistance change with frequency in a SPIM is the double cage rotor slot design. The double cage rotor slot geometry generally consists of two separate conductive bars; the top bar is round and the bottom bar is pear-shaped, as in Figure 1(b).

The structure of the double cage rotor slot and its equivalent circuit are shown in Figure 4(a) and Figure 4(b), respectively. In the equivalent circuit, R_{ro} and R_{ri} indicate resistance of the rotor upper and lower bar, X_{ro} and X_{ri} indicate the reactance of the rotor upper and lower bar, and X_m is the mutual inductance between the rotor lower and upper bar.

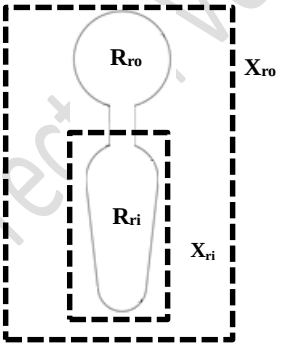

(a)

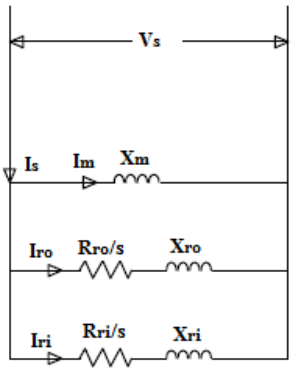

(b)

Figure 4. (a) Double cage rotor and (b) Rotor equivalent circuit

In the double cage rotor slot geometry, the rotor upper bar is effective during the start of the motor and the rotor lower bar in steady-state operation. The inductance of the rotor upper bar. (L_{bo}) in a motor with double cage rotor slot structure is calculated using Equation (8) [13].

$$L_{bo} = \mu_0 . l_{br} . N_r^2 . \lambda_{bo} \quad (8)$$

The coefficient of permeability (λ_{bo}) presented in Equation (8) is calculated using Equation (9).

$$\lambda_{bo} = 0.66 + \frac{h_{or}}{B_{s0}} \quad (9)$$

The rotor lower bar inductance (L_{bi}) is effective at the time of rated operation and is calculated using Equation (10).

$$L_{bi} = \mu_0 . l_{br} . N_r^2 . \lambda_{bi} \quad (10)$$

The coefficient of permeability (λ_{bi}) in Equation (10) is calculated using Equation (11), where k_3 varies between $1 < k_3 < 2$ in the related Equation [8].

$$\lambda_{bi} = \frac{H_{s2}}{3B_{s1}} k_1 + k_3 + \frac{H_{s3}}{B_{s3}} + \frac{h_{or}}{B_{s0}} \quad (11)$$

The reactance of the rotor upper bar is calculated using Equation (12), using the rotor upper bar inductance (L_{bo}) from Equation (8).

$$X_{ro} = 2\pi f L_{bo} \quad (12)$$

The reactance of the rotor lower bar is calculated using Equation (13), using the rotor lower bar inductance (L_{bi}) from Equation (10).

$$X_{ri} = 2\pi f L_{bi} \quad (13)$$

The impedance of the upper and lower bars are calculated using Equation (14) and Equation (15), respectively. R_{ro} and R_{ri} are the electrical resistance of the upper bar and lower bar, respectively [13].

$$Z_{ro} = \frac{R_{ro}}{s} + jX_{ro} \quad (14)$$

$$Z_{ri} = \frac{R_{ri}}{s} + jX_{ri} \quad (15)$$

The total impedance of the rotor circuit (Z_t) is calculated using Equation (16). R_{sm} and X_{sm} are the stator main winding resistance and the stator main winding leakage reactance, respectively.

$$Z_t = \frac{Z_{ro} . Z_{ri} . X_m}{Z_{ro} + Z_{ri} + X_m} + R_{sm} + jX_{sm} \quad (16)$$

The input current (I_s) is calculated using Equation (17) by using the total impedance, Z_t, and phase voltage of the rotor circuit, V_s.

$$I_s = \frac{V_s}{Z_t} \quad (17)$$

The equations show that slot depth causes varying effects on electrical parameters. This study therefore investigates an optimal deep slot motor design derived from references [14-16] that has been implemented as a motor model for analysis in the Ansys / Maxwell FEA software and constructed as a prototype for measurement.

2.3 Finite element method (FEM)

This study uses a 3-dimensional numerical model of a SPIM for which the electrical and magnetic properties are known, that has been developed using the ANSYS / Maxwell program based on the finite element method (FEM). The program has created mesh structure of the stator and the rotor (Figure 5(a)) and rotor bars (Figure 5(b)). The mesh structure is made up of elements which contain nodes that represent the shape of the geometry.

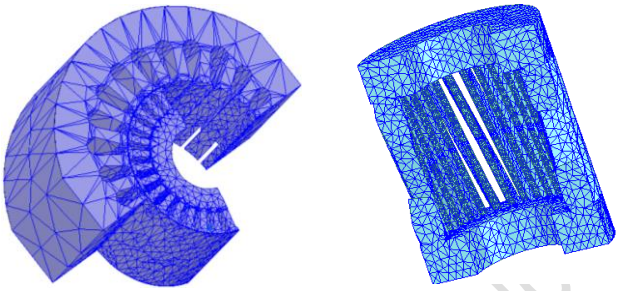

(a) (b)

Figure 5. Mesh process completed model view (a) Stator and rotor (b) Rotor cage

2.4 Rated load performance of SPIM models

Motor performance has been evaluated through 2D FEM analysis of a SPIM. Three rotor models were created: the original motor model (Model A), deep slot (Model B) and double cage (Model C). The models were further analyzed using 3D FEM for 0.5 seconds for greater accuracy in the analysis and to make accurate comparison. The finite element models are shown as Figure 6(a) for Model A, Figure 6(b) for Model B and Figure 6(c) for Model C.

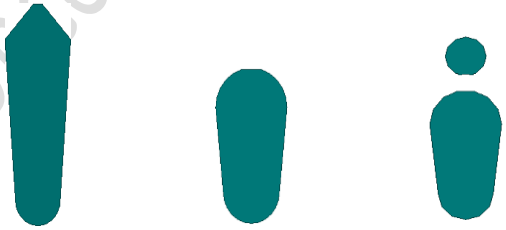

(a) (b) (c)

Figure 6. Finite element models (a) Model A, (b) Model B and (c) Model C

Table 1. Rotor slot geometric dimensions of model A, model B and model C

Rotor Slot Parameter	Model A	Model B	Model C
Number of rotor slots, N_r	30	30	30
Slot top Width, B_{s1}	3.15 mm	3.71 mm	3.5 mm
Slot bottom width,B_{s2}	2.14 mm	2.914 mm	2.68 mm
Slot mouth width, B_{s0}	0.4 mm	1.0 mm	0.75 mm
Slot depth H_{s2}	6.92 mm	4.0 mm	3.61 mm
Slot shape	Conical	Pear	Double cage
Slot distance $Hs0$	0.2675 mm	0.2 mm	0.2 mm
Slot skew angle	15˚	15˚	15˚

Slot opening	Close	Close	Close
Slot neck upper Radius, r	-	-	-

The rotor slot geometric dimensions given in Table 1 were obtained by parametric analysis in the Ansys/Maxwell program. In the Ansys/Maxwell program, parametric analysis was performed by defining a certain data range for each rotor slot parameter under the criteria of geometric dimensions of the stator, geometric dimensions of the rotor, and the length of the air gap between the rotor and stator air. Each of the rotor slot geometries was given a constant total rotor slot area (A_r = 21.856 mm^2) by selecting appropriate values for the rotor lower (B_{s1}) and upper (B_{s2}) slot widths. Moreover, as the width of the lower and upper of the rotor slot is changed, the parallelism of the rotor slot teeth is preserved.

The rotor slot sizes that provide the best motor performance within a certain data range have been determined as the optimal value. And this step was repeated for all rotor slot parameters presented in Table-1.

M470-50A siliceous sheet is defined as the core material in the rotor. The onset of saturation of this sheet is 1.71 T. Advantage was taken of the symmetrical structure of the SPIM and analysis was undertaken on the half model.

2.5 The excitation circuit of SPIM

The excitation circuit for motor start up is shown in Figure 7. It consists of the main and auxiliary windings connected parallel to each other. R_{sm}, L_{ecm} and L_{sm} in succession the resistance of the main winding, end-winding inductance and winding phase inductance. R_{sa}, L_{eca} and L_{sa} represent the resistance, end-of-winding inductance, and phase inductance of the auxiliary winding, respectively. The difference of phase inductance is that it relies on the magnetic flux. The run capacitor (C) connected in series with the auxiliary winding and in parallel to the starting resistance (R_s) is shown in Figure 7. The auxiliary winding is maintained on by the run capacitor, increasing the power from the motor and reducing the reactive power, with the power factor approaching a value of 1. When the motor reaches 2800 rpm, the starting resistance (R_s) is then took out the switch and the auxiliary winding remains on via the capacitor.

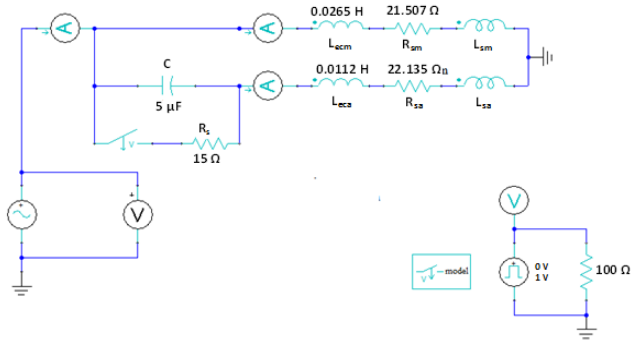

Figure 7. The excitation circuit of a SPIM

3 Results and discussion

The torque-speed curve of induction motors is important in determining motor performance. This curve provides technical information such as the change of the speed of the motor under different loading conditions, and the speed at which the breakdown torque occurs and the synchronous speed cannot be achieved [12] Model A, Model B and Model C were loaded up to 1 Nm in 0.1 Nm steps starting from 0 Nm, with the torque-speed curves for each motor under different loading conditions shown in Figure 8.

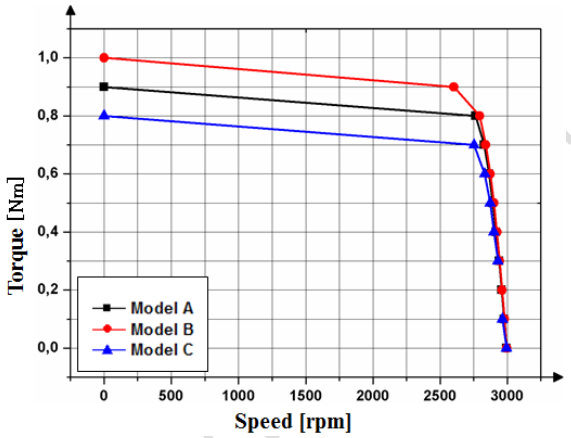

Figure 8. Comparison of torque-speed curves

The torque-speed curves show that Model A has a breakdown torque of T_d = 1 Nm, Model B has a breakdown torque of T_d = 1.02 Nm and Model C has a breakdown torque of T_d = 0.93 Nm. The motor performance data obtained from the 3D FEM analysis for the different slot geometries of the rotor are given in Table 2.

Table 2. Comparison of performance data obtained from 3D FEM

Performance Parameters	Model A	Model B	Model C
Input Power (W)	177.12	170.8	166.2
Output Power (W)	127.97	128.2	128.4
Efficiency (%)	71.8	75.05	75.52
Current (A)	0.976	0.882	0.84
Power Factor (cos φ)	0.83	0.88	0.92
RatedTorque (Nm)	0.42	0.42	0.42
Speed (rpm)	2911	2918	2921
Slip (%)	2.96	2.73	2.63

Table 2 shows the output power was approximately equal for all models. This is because the load torque and speed are approximately equal. However, there is a decrease in the input power for the B and C model slot type. This is because the current decreases as the power factor of the motor increases. The power factor changes due to the decrease in the magnetizing current, the length of the flux path due to the depth of the groove, and the change in the reluctance and thus the

inductance. Table 2 shows the efficiency of Model B with deep slot structure is increased by 4.53% and the efficiency Model C with double cage slot is increased by 5.18%.

3.1 Tests of the SPIM

The accuracy of the Finite Element Analysis was verified by comparing with the electrical and mechanical measurements from prototype precision models of the deep slot and double cage rotor slot motors (Figure 9). The stator of all 3 models was the same.

(a) (b)

Figure 9. Prototype model of the stator and rotor of SPIM (a) Front view and (b) Side view

An experimental test system was measured performance of prototype motor that was sufficiently accurate to compare with the simulation data (Figure 10). The test system consists of load and drive systems with capabilities to examine the electrical and mechanical behavior of the SPIM under different loading conditions. The test system (FESTO Drive Lab) consists of an servo motor, power transmission components (shafts, couplings). Prototype motor is loaded by servo motor which is measure from electromagnetic torque. Test system control and data acquisition carry out by Drive Lab software. Motor torque and speed are obtained from test system, voltage, current, power factor are measured by digital wattmeter, temperature is measured by digital thermometer. Winding resistance is measured by digital multimeter.

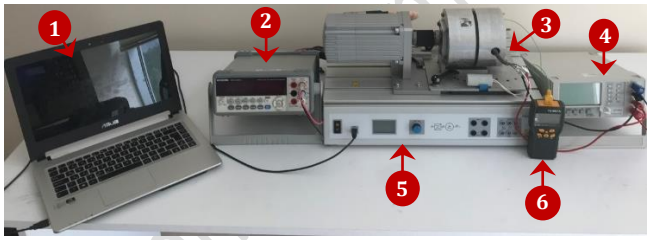

Figure 10. Test setup used in laboratory measurements (1-Computer, 2-Multimeter, 3-SPIM, 4-Wattmeter, 5-Test device, 6-Thermometer)

The measurement system shown in Figure 10 was used to obtain the torque-speed curves of the Model A, Model B and Model C prototype motors by recording the speed under various loading conditions. The motors were loaded up to the breakdown torque after reaching the working temperature for each model. The load torque was then reduced in 0.1 Nm steps, and tested up to no load operation. Measurements were made by keeping the motor under constant load for 2 minutes at each loading step. The behavior of the temperature of the motors to reach the thermal equilibrium over time under the rated load is shown in Figure 11.

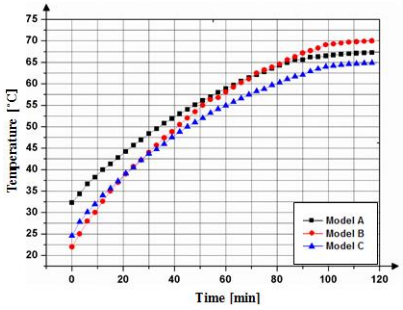

Figure 11. Time dependent curves of winding temperatures of Model A, Model B and Model C during the experiment

Figure 11 shows the time dependent variation of winding temperature of Model A, Model B and Model C under full load. The motors reach the working temperature of 65-70 C after approximately 100 minutes.

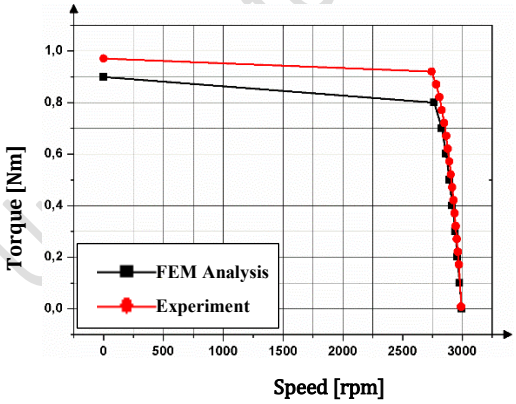

(a)

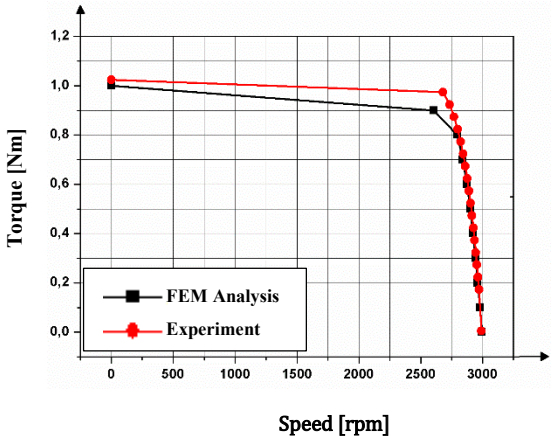

(b)

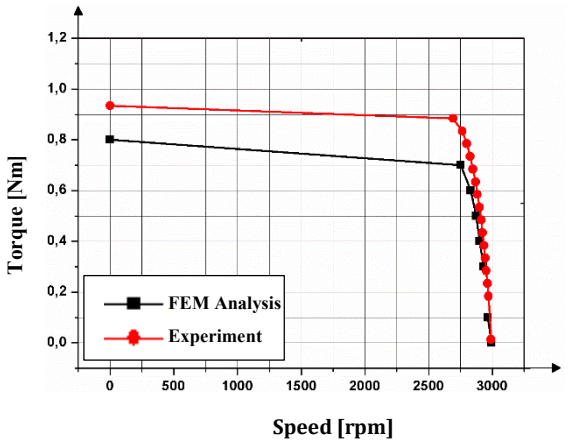

(c)

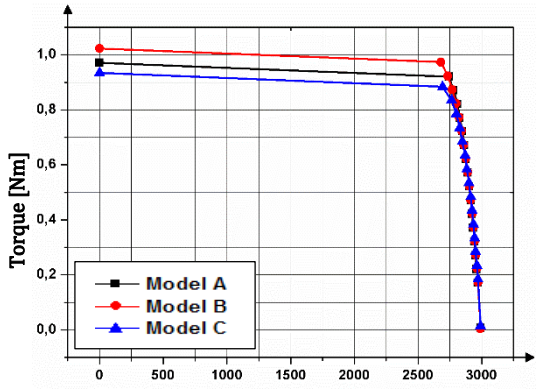

(d)

Figure 12. Torque-speed curve of (a) Model A, (b) Model B, (c) Model C and (d) Comparison of torque-speed curves obtained from experimental results

Figures 12(a), 12(b) and 12(c) compare the torque-speed curves for each model of motor, Model A, Model B and Model C, for the simulation and experimental methods. The results have close agreement for speed over most of the torque range, however the value for breakdown torque was somewhat higher in the experimental method compared to simulation. The torque-speed curves for Model A, Model B and Model C in Figure 12(d) show the breakdown torque for Model A was s_d = 0.92 Nm, breakdown torque for Model B was s_d = 0.98 Nm, and breakdown torque for Model C was s_d = 0.89 Nm.

The results from the 3D FEM analysis and experimental measurement for the three slot geometries of the rotor are given in Table 3. According to Table 3, it can be seen that there are small differences between the simulation and experimental results. In simulation studies conducted using FEM, efforts are made to generate a model that closely resembles the actual model. However, the utilization of the mathematical model of the motor, minor measurement errors, and the assumption of ideal conditions for all environmental factors and materials used constitute the rationale behind the disparities between simulation and experimental results. Since the electric motor used in the study was a small powerful motor, small differences between simulation and experimental results led to significant result differences.

The electric motor used in this study is a small powerful motor.

Table 3. Comparison of performance results obtained from 3D FEM analysis and experimental measurement

Performance Parameters	MODEL A		MODEL B		MODEL C	
	Test	3D FEM	Test	3D FEM	Test	3D FEM
Input Power (W)	176.8	177.12	171.9	170.8	167.5	166.2
Output Power (W)	128.6	127.97	128.6	128.2	128.9	128.4
Efficiency (%)	72.86	71.8	74.81	75.05	76.96	75.52
Current (A)	0.98	0.976	0.92	0.882	0.81	0.84
Power Factor (cos φ)	0.82	0.83	0.85	0.88	0.94	0.92
Rated Torque (Nm)	0.42	0.42	0.42	0.42	0.42	0.42
Speed (d/d)	1	0.9	1.02	1	0.92	0.8
Slip (%)	2.93	2.91	2.93	2.92	2.93	2.92
Breakdown Slip (%)	2.48	2.96	2.47	2.73	2.532	2.63
Max. Temperature (°C)	13.1	13	13.6	13.5	13.8	13.74
Ambient temperature (°C)	20	20	20	20	20	20

Results from 3-D finite element analysis and experimental measurement are given in Table 3. The output power for the three slot shapes was approximately equal and is explained by the load torque being constant and the rated speed is approximately equal. However, the input power for the B and C model slot type is less than model A. This is because the current decreases as the power factor of the motor increases due to the decrease in the magnetizing current and change of the reluctance and inductance as a result of the lengthening of the flux path due to the depth of the slot.

The decreased current results in reduced copper losses in the windings and increased efficiency of the motor. The experimental data shows that the efficiency of the Model B motor with deep slot structure increased by 1.95% and the Model C motor with double cage slot structure increased by 4.1%. However, the breakdown torque decreases and the breakdown slip increases compared to the original model. The ratio of breakdown torque to rated torque is 2.19 for Model C, 2.38 for Model A and 2.43 for Model B. The ambient temperature of the testing environment is 20 °C. The operating temperature was obtained with a thermocouple immersed in the stator windings. The stator windings used in this motor are aluminum material with a thermal conductivity coefficient of approximately 237 W/mK.

The working temperature was calculated as 75 °C in the simulation and was measured to be 69-76 °C in the

experiments. The small differences between the temperatures have been neglected.

4 Conclusion

This study investigates the increase in motor performance that arises from optimizing the rotor slot geometry of a permanent capacitor SPIM used as a refrigerator compressor. 3D analysis models of three rotor designs, the original rotor slot model of SPM (model A), deep slot (Model B) and double cage rotor slot model (Model C), were developed and electromagnetic simulation performed. Prototypes of the deep slot (Model B) and the double cage rotor slot model (Model C) were produced to match the geometries of the simulation models and experimental results obtained for comparison. The simulation and experimental results were in close agreement and confirm findings. The experimental measurements show that the motor efficiency for the deep slot (Model B) increased by 1.95%, and the efficiency for the double cage (model C) increased by 4.1%.

The experimental measurements found the characteristics of the model B and model C motors under continuous operation (S1) mode with supply voltage 220 V ac were; spindle torque: 0.42 Nm, output mechanical power: 125 W (1/6 BG), and efficiency: 77%.

Electric motors are categorized into 4 different classes as IE1, IE2, IE3 and IE4 by the European Electrotechnical Standardization Committee according to their efficiency values [17]. However, this classification only covers electric motors with a power of greater than 0.75kW motors such as the one discussed in this study are not included in any efficiency class.

However, today, this type of motor is widely preferred in domestic and low-power industrial applications. Although these types of motors are ignored in energy consumption, they cause significant energy consumption due to their widespread use. Further classes of refrigerator energy use will be required if a double cage motor with an increased efficiency of 4.1% is used as the refrigerator compressor motor. Although a double cage motor will increase the cost of the product, it will reduce energy consumption, and thus total cost of ownership. Moreover, changing the motor to rotor slot form is easy to accomplish in the manufacture process as it does not require any change in the aluminum injection operation and so requires little additional investment in the production process.

5 Author contribution statements

All authors contributed to the study conception and design. Literature review, model design, data collection and all analysis were performed by Author 1. The study was supervised by Author 2. The first of manuscript was written by Author 1 and all authors commented on previous versions of manuscript. All authors read and approved the final manuscript.

6 Ethics committee approval and conflict of interest statement

No need for permission from ethics committee for the article prepared. There is no conflict of interest in the article prepared.

7 References

[1] Mademlis C, Kioskeridis I, Theodoulidis T. "Optimization of single-phase induction motors-part I: maximum energy efficiency control". *IEEE Transaction on Energy Conversation*, 20(1), 187-195, 2005.

[2] Matic D, Kanovic Z. "Vibration based broken bar detection in induction machine for low load conditions". *Advances in Electrical and Computer Engineering,* 17(1), 49-54, 2017.

[3] Park YS. "Investigation on electromagnetic performance of induction motor with rotor bar faults considering motor current signals". *Advances in Electrical and Computer Engineering*, 20(4), 37-44, 2020.

[4] Chapman SJ. *Electric Machinery Fundamentals*, 5th ed., New York, USA, McGraw-Hill, 2011.

[5] Iqbal MA, Singh G. "A review on influence of rotor geometry on the performance of single-phase capacitor-run induction motor". *International Journal of Advanced Research in Electrical, Electronics and Instrumentation Eng*ineering, 3(6), 10216-10224, 2014.

[6] Rui Z, Qunjing W, Guoli L, Cong P, Guanghui F. "Optimal design of single-phase induction motor based on Maxwell 2D Rmxprt". *International Conference on Electrical Machines and Systems*, Incheon, South Korea, 10-13 October 2010.

[7] Akhtar MJ, Behera RK, Parida SK. "Optimized rotor slot shape for squirrel cage induction motor in electric propulsion application". *Proceedings of the 6th India International Conference on Power Electronics,* Kurukshetra, India, 8-10 December 2014.

[8] Sobhani S, Yaghobi H, Samakoosh M. "Optimize efficiency and torque in the single-phase induction motor by adjusting the design parameters". *Proceedings of the 12th International Conference on Environment and Electrical Engineering*, Wroclaw, Poland, 5-8 May 2013.

[9] Fireteanu V, Tudorache T, Turcanu OA. "Optimal design of rotor slot geometry of squirrel-cage type induction motors". *IEEE International Conference on Electric Machines & Drives,* Antalya, Turkey, 03-05 May 2007.

[10] Yahaya EA, Omokhafe T, Agbachi EO, James AG. "Advantage of double cage rotor over single cage rotor induction motor". *International Journal of Innovative Systems Design and Engineering,* 6(12), 1-4, 2015.

[11] Şen Kurt M, Fenercioğlu A. "Effect of the variable resistance rotor slot design on the performance of the single phase asynchronous motor (SPAM)". *Sigma Journal of Engineering and Natural Sciences Effect of the Variable Resistance*, 38(1), 213-226, 2019.

[12] Şen Kurt M, Fenercioğlu A. "Rotor slot distance effects on output parameters in single phase induction motors", *Hittite Journal of Electrical Engineering,* 5(1), 31-35, 2018.

[13] Fenercioğlu A, Şen Kurt M, Akar M, Kurt, Ü. "Double cage rotor bar structure influences on performance of the single phase induction motor". *International Symposium on Multidisiplinary Studies and Innovative*, Tokat, , Turkey, 02-04 November 2017.

[14] Şal S, İmeryüz M, Ergene LT. "Kafesli asenkron motorlarda maliyet kisiti altinda rotor çubuklarinin analizi". *Emo Bilimsel Dergi,* 2(3), 23-28, 2012.

[15] Bal G. *Özel Elektrik Makinaları*, 4th ed. Ankara, Turkey, Seçkin Press, 2011.

[16] Fitzgerald AE, Kingsley JC, Umans SD. *Electric Machinery*, 6th ed. Bostan, USA, Mcgraw-Hill, 2003.

[17] Ferreira FJTE, Silva AM, Almeida AT. "Single-Phasing protection of line-operated motors of different efficiency classes", *IEEE Transactions on Industry Applications*, 54(3):, 2071-2084, 2018.